PCCP

PAPER

View Article Online
View Journal



Cite this: DOI: 10.1039/c7cp07051a

# Quantitative biosensor detection by chemically exchanging hyperpolarized $^{129}$Xe†

S. Korchak,‡[a] T. Riemer,[b] W. Kilian[a] and L. Mitschang ‡*[a]

Chemical sensors informing about their local environment are of widespread use for chemical analysis. A thorough understanding of the sensor signaling is fundamental to data analysis and interpretation, and a requirement for technological applications. Here, sensors explored for the recognition and display of biomolecular and cellular markers by magnetic resonance and composed of host molecules for xenon atoms are considered. These host–guest systems are analytically powerful and also function as contrast agents in imaging applications. Using nuclear spin hyperpolarization of $^{129}$Xe and chemical exchange saturation transfer the detection sensitivity is orders of magnitude enhanced in comparison to conventional $^{1}$H NMR. The sensor signaling reflects this rather complex genesis, furthering the mere qualitative interpretation of biosensing data; to harvest the potential of the approach, however, a detailed numerical account is desired. To this end, we introduce a comprehensive expression that maps the sensor detection quantitatively by integration of the hyperpolarization generation and relaxation with the host–xenon exchange dynamics. As demonstrated for the host molecule and well-established biosensor cryptophane-A, this model reveals a distinguished maximum in sensor signaling and exerts control over experimentation by dedicated adjustments of both the amount of xenon and the duration of the saturation transfer applied in a measurement, for example to capitalize on investigations at the detection limit. Furthermore, usage of the model for data analysis makes the quantification of the sensor concentration in the nanomolar range possible. The approach is readily applicable in investigations using cryptophane-A and is straightaway adaptable to other sensor designs for extension of the field of xenon based biosensing.

Received 16th October 2017,
Accepted 18th December 2017

DOI: 10.1039/c7cp07051a

rsc.li/pccp



## Introduction

The noble gas xenon is of broad interest in chemistry as a versatile agent for the probing of molecular environments. The inert atoms associate through noncovalent interactions with hydrophobic cavity-like structures, being of natural origin like in the interior of biomacromolecules and in bacterial spores,[1–4] or synthetic as inside engineered protein sites[5,6] or supramolecular xenon host molecules[7–9] and in the pores of nanomaterials.[10,11] The states of free and cavity-bound xenon are mapped by NMR as the xenon magnetic resonance frequency exhibits a fine response to the local molecular structure due to a large chemical shift dispersion.[12] Moreover, the spin −1/2 isotope $^{129}$Xe can be hyperpolarized by spin exchange optical pumping to an up to five orders of magnitude larger signal amplitude than in the conventionally utilized thermal equilibrium in high magnetic field.[13] NMR on hyperpolarized $^{129}$Xe (hpXe) thus enables the inspection of rare species and events where low spin density but high detection sensitivity are imperative. The approach is presently developed further for the detection of biomarkers at the micro- to nanomolar concentration levels *in vitro* and possibly *in vivo*.[14–18] Such biosensing uses xenon accessible sensor molecules which allow on the one hand targeting of the markers but also to take advantage of ultra-sensitive NMR. Herein, the detection of biosensors using hpXe is evaluated in detail to further the understanding of signal formation, to enable methodological improvements, and to reach a quantitative assessment of the biosensing approach.

Biosensing is facilitated by molecular host structures where hpXe is transiently enclosed and thus experiences an alteration of its magnetic resonance frequency. By unspecific or, through functionalization, specific association of the host with the molecular or cellular marker of interest the host–hpXe system acts as a sensor or contrast agent that is indicative of the marker substance.[19,20] The NMR readout may be either direct by acquisition of the signal from host-bound hpXe or indirect

[a] *Physikalisch-Technische Bundesanstalt (PTB), Abbestr. 2–12, 10587 Berlin, Germany. E-mail: Lorenz.Mitschang@ptb.de*
[b] *University of Leipzig, Medical Department, Institute of Medical Physics and Biophysics, Härtelstr. 16–18, 04107 Leipzig, Germany*

† Electronic supplementary information (ESI) available: Specification of exchange rates, association constant, hyperpolarization parameter; calculation of HyperCEST effect; determination of maxima positions. See DOI: 10.1039/c7cp07051a

‡ Authors contributed equally to the work.

by the chemical exchange saturation transfer method, termed Hyper-CEST when referring to hpXe.[21] In Hyper-CEST the magnetization of host-bound hpXe is continuously selectively destroyed, *e.g.* saturated by radiofrequency (RF) irradiation. Because of the repeatedly renewed binding to the host, the magnetization of unbound hpXe is also diminished. The contrast agent can thus be detected largely amplified by the Hyper-CEST effect, *i.e.* the difference in signal intensity of unbound hpXe when saturation transfer is effective or not. The presence and activity of specific biomarkers in solution could thus be approved by the mere generation of the Hyper-CEST effect using dedicated molecular sensors.[22–26] It is, nonetheless, highly desirable to extent biosensing for quantitative explorations. The determination of the contrast agent concentration or of its modulation would enable quantitative biomolecular analytics *in vitro* and were a prerequisite for quantitative molecular imaging applications. A quantitative understanding of the host–guest interaction would also help improve sensor design and benchmarking with the aim to identify the best choice for a particular application. Quantitation by Hyper-CEST, however, is a formidable task because the detection is indirect and, at any point of time, relates to only a fraction of all contrast agent due to a limited host–hpXe binding affinity.

While the operational saturation transfer has been detailed,[27] an account of the integral detection process is challenging owing to the intricate interplay of the xenon polarization generation, the spin relaxation, and the host–hpXe exchange dynamics. In particular, the amount of hpXe used for sensing is not adequately considered so far. This quantity, which is like the applied RF saturation in principle under control of the experimenter, can substantially affect the outcome of measurements through the achievable spin polarization, the free and host-bound xenon equilibrium concentrations, and the exchange rate.[28–31] It is thus not evident how to conduct sensing experiments for maximum contrast or at the limits of detection. Furthermore, quantitative explorations have only recently been initiated with the emphasis on the numerical specification of parameters relevant to the sensing approach, *e.g.* the exchange kinetics rate coefficients and the host–hpXe affinity.[31–34] In particular, the fraction of host molecules occupied by hpXe has been determined using Hyper-CEST data with a variation in saturation offset (so called Z-spectra) and power.[35] By this approach, the respective absolute concentration of occupied hosts is only possible to derive when the total concentration of host molecules is known and taken into account. This latter quantity is the relevant one concerning the binding of the sensor to the biomarkers and, thus, for quantitative biosensing applications. Strategies for the determination of the generally unknown total contrast agent concentration, however, are lacking.

We thus set out by taking explicitly reference of the xenon concentration in addition to the duration of the saturation transfer as the means for manipulation and steering in biosensing measurements. By specification of the parameters describing the xenon polarization generation, the relaxation and the exchange with the host, we eventually arrive at a quantitative model for the biosensor detection. This model should make apparent any extremal sensor performance, which could then be experimentally probed, and could also suggest strategies for the quantification of the total contrast agent concentration by the Hyper-CEST effect. We chose for demonstration purposes the host molecule cryptophane-A (CrA) which is well understood in terms of the xenon binding interaction[8,31,36–39] and well established as a biosensor for protein and cellular markers.[14–16,19–23]

## Results

### The model

The experimental situation we are exploring is displayed in Fig. 1. The host molecule, *e.g.* CrA, and the xenon guest molecules combine and dissociate rapidly in solution at rates $k_{on}$ and $k_{off}$, respectively (Fig. 1A). The magnetization of the freely dissolved xenon is effectively diminished by saturation transfer when the host-bound hpXe is selectively irradiated (Fig. 1B lower spectrum).

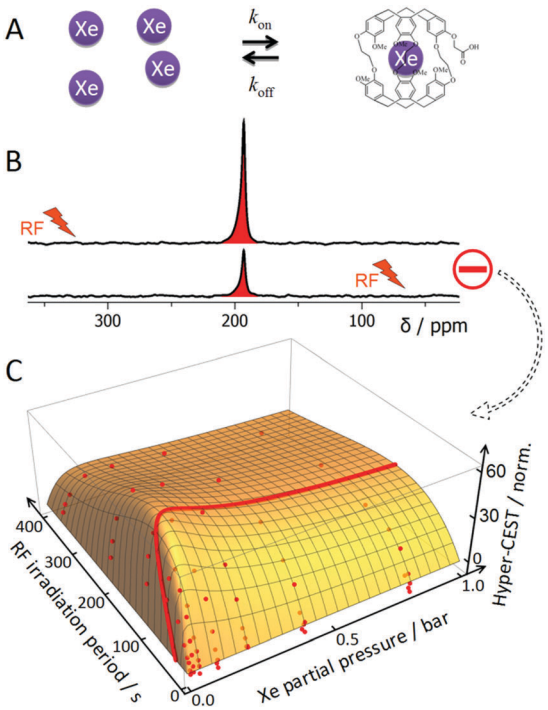


Fig. 1 Experiment and data evaluation scheme. (A) In solution hpXe binds reversibly to the host (CrA). (B) The saturation of the magnetization of host-bound hpXe by resonant RF irradiation (lower trace) leads to a diminished free hpXe signal in comparison to the case for off-resonant irradiation mirror-symmetrical with respect to the free xenon signal (upper trace). The free hpXe (here 86 μM) generates a strong signal at 196 ppm in either case while for the 90 nM CrA used here the signal from host-bound hpXe at 65 ppm is not visible. (C) The difference between signal intensities for off-resonant and resonant RF irradiation (Hyper-CEST effect) can be mapped in dependence of the xenon gas partial pressure (or free xenon concentration) and the RF irradiation period. Experimental data for CrA in water at 298 K (red dots) are superimposed onto the plot of the function $S(\rho,\tau)$ solely scaled by a global fit parameter else evaluated for the parameters given in Table 1 and for a host concentration of 90 nM. The crest line (red) indicates for given xenon partial pressure the maximum Hyper-CEST effect. The normalization is by the maximum Hyper-CEST effect for 0.9 nM CrA at 298 K (also used in Fig. 2A and Fig. S4, ESI†).

To reference this depletion solely due to saturation transfer, a second experiment is conducted in an identical manner but with the RF irradiation applied at a position mirror-symmetrically with respect to the free xenon signal (Fig. 1B upper spectrum). In this case, saturation transfer does not occur but any effect of direct saturation of the bulk signal possibly induced by the RF irradiation and the always immanent relaxation are accounted for. The model

$$S(\rho,\tau) = A(\rho)\exp\{-R\tau\}[1-\exp\{-k_{on}(\rho)\tau\}] = \frac{\rho}{1+\alpha\rho/s}\exp\{-R\tau\}\left[1-\exp\left\{-(c+k\rho)\frac{KC}{1+K\rho}\tau\right\}\right] \quad (1)$$

is introduced here for describing the Hyper-CEST effect as the difference in the signal intensities from both experiments. The variables are the concentration of freely dissolved xenon $\rho$ and the duration of the RF irradiation period $\tau$. Practically, the solution is saturated with hpXe, *e.g.* by gas bubbling, such that by Henry's law $\rho = sp$ for xenon solubility $s$ and partial pressure $p$, the latter is thus a variable for $S$ equivalently to $\rho$. The leading amplitude factor $A(\rho)$ is the initial ($\tau = 0$) free xenon magnetization density in the solution which reflects the $^{129}$Xe hyperpolarization process (ESI†). The term $A(\rho)\exp\{-R\tau\}$ then represents the signal intensity when saturation transfer is not effective. The rate $R$ comprises two contributions, one due to spin relaxation and one due to possible direct saturation effects from the RF irradiation.[27] Strictly speaking, because both processes occur at different rates for free and host-bound xenon, $R$ comprises an exchange averaged rate given by the population weighted – and thus $\rho$-dependent – mean of the rates of encaged and free xenon, respectively. However, due to the low host concentration in biosensing applications, like the ones probed in this work, practically only the free xenon pool is relevant for $R$. The remaining term in the model, $A(\rho)\exp\{-R\tau - k_{on}(\rho)\tau\}$, represents the free xenon signal intensity when saturation transfer is effective. In addition to $R$, the chemical exchange driving the saturation transfer enters the model *via* the rate for complex formation, $k_{on}(\rho)$.[34] In dynamic equilibrium the magnetization leakage from the pool of free xenon due to exchange occurs with rate $-k_{on}(\rho)$, assuming complete saturation of host-bound spins. This dependence on $k_{on}(\rho)$ also derives from an analytical approximate solution of the Bloch–McConnell equation for complete saturation of the host-bound xenon spins by resonant irradiation.[27]

A global amplitude factor is not explicitly stated in the model. It is evident that, depending on the experimental setup at hand, only a fraction of the originally generated $^{129}$Xe polarization is available in the sample for the NMR experiment. Also, the signal intensities in absolute terms which contribute to the Hyper-CEST effect are derived from spectra acquired on a particular NMR instrument. It is thus required to obtain the overall amplitude of the model by normalization with respect to the experimental data.

The explicit functional form of $S(\rho,\tau)$, derived in the ESI,† depends on a number of parameters: $\alpha$ describes the alkali metal spin destruction by collisions with xenon during the hyperpolarization process, $c$ is the host–xenon complex dissociation rate coefficient, $k$ is the rate coefficient for degenerate xenon exchange, $K$ is the complex association constant, and $C$ is the total host concentration in the solution. We determined the hyperpolarization and exchange parameters ($\alpha$, $c$, $k$, $K$) by dedicated experimentation independently from the Hyper-CEST approach (Experimental section, ESI†). Importantly, such measurements can be done at much higher host concentration than used in future applications while the results remain valid as long as the sample temperature and the solution conditions are kept. The rate $R$ was derived from the variant of Hyper-CEST (or part of data) where signal decay is observed without the saturation transfer effective. Concerning the xenon solubility $s$, the Ostwald coefficient is tabulated, particularly for water, physiologically relevant solutions, and body fluids based on the early use of the radioactive xenon-133 in medicine.[40–42] The parameters for the CrA–hpXe host–guest system in aqueous solution at the two temperatures of 298 K and 310 K are compiled in Table 1.

## Sensor performance

The validity of the model characterizing the sensor signaling was tested by comparison with experimental results. A solution of 90 nM of the water-soluble derivative monoacetic acid cryptophane-A in pure water was saturated with hpXe gas at 298 K. A total number of 70 experiments for either type of experiment – saturation transfer effective or not – were conducted using for the xenon partial pressure $p$ seven constant settings in between 0.01 bar and 0.8 bar (amounting to a range of 43 μM to 3.5 mM for the free xenon concentration) and, for each such fixing, the irradiation period $\tau$ was varied in ten steps in between 0 s and 350 s. For comparison, the model was evaluated over a similar range for both variables, $\rho$ and $\tau$, using the parameters listed in Table 1. Only the global amplitude of $S(\rho,\tau)$ was adjusted in a least-squares minimization to the experimental data to account for instrumentation related scaling. It is evident from Fig. 1C that the model reproduces the measurements well. The match of model and measurements may be quantitatively assessed by the coefficient of variation of 0.15. In this example, the model and the experimental data are a rather smooth function in both variables with a soft curvature along $\tau$, and a steeper one along $p$. Remarkable is the single, global maximum which is located

Table 1 Parameters for monoacidic acid CrA and hpXe in water

| Temp. (K) | $s$/Mbar$^{-1}$ | $\alpha$/bar$^{-1}$ | $R$/s$^{-1}$ | $c$/s$^{-1}$ | $k$/M$^{-1}$ s$^{-1}$ | $K$/M$^{-1}$ |
|---|---|---|---|---|---|---|
| 298 | 0.00432 ± 0.00006 | 8.36 ± 0.76 | 0.00662 ± 0.00012[a] | 20.0 ± 0.3 | 5800 ± 280 | 58 400 ± 6800 |
| 310 | 0.00325 ± 0.00003 | 8.36 ± 0.76 | 0.00494 ± 0.00014 | 74.1 ± 2.5 | 12 400 ± 2600 | 28 900 ± 2200 |

[a] $R$ = 0.00594 ± 0.0002 s$^{-1}$ for the samples of the dilution series at 298 K.

at the position $p_{max}$ = 74 mbar and $\tau_{max}$ = 108 s. For this sample and the used instrumentation, it marks the performance of the maximum Hyper-CEST effect.

The topology of the surface $S(\rho,\tau)$, or the performance of the sensor, is governed by the saturation transfer rate, as the relaxation and direct saturation rate $R$ as well as the polarization amplitude $A(\rho)$ contribute in an identical manner to either of the subtracted signal intensities. The dependence of $k_{on}(\rho)$ on the kinetic rate coefficients and the binding constant, however, makes the Hyper-CEST effect specific to the host–guest interaction at the molecular level and, thus, dependent on the particular host molecule used and the temperature. Moreover, a strong response in $S(\rho,\tau)$ can be expected for changes of the total host concentration which is linked to $k_{on}$ by direct proportionality. For demonstration, the model was evaluated for various host concentration at 298 K as well as at 310 K using the parameters from Table 1 (ESI,† Fig. S4). Evidently, the overall topology changes mainly due to the relocation of the maximum which moves towards larger irradiation period but smaller xenon partial pressure when the host concentration decreases. The Hyper-CEST effect at given host concentration is comparatively stronger at the higher temperature which is attributed to the higher exchange rate. However, at given temperature, the Hyper-CEST effect decreases steadily along with the host dilution because of a diminishing exchange rate.

### Detection limit

For the achievement of the maximum Hyper-CEST effect experiments need to be conducted at the proper settings for the xenon concentration, $\rho_{max}$, and the irradiation period, $\tau_{max}$. We could calculate $\rho_{max}$ and $\tau_{max}$ for finite host concentration by $S(\rho,\tau)$ semi-analytically (ESI†). In Fig. 2A the xenon partial pressure and the irradiation period for maximum Hyper-CEST effect for the host concentrations of 900 nM, 90 nM, 9 nM, and 0.9 nM at 298 K and 310 K, respectively, are displayed. Apparently, the maxima loci move towards a converging point for ever smaller host concentration whose position can be derived from $S(\rho,\tau)$ (ESI†). For vanishing $C$ the maximum occurs at $p_{max}$ = 24 mbar, $\tau_{max}$ = 151 s for 298 K and $p_{max}$ = 38 mbar, $\tau_{max}$ = 202 s for 310 K, respectively. At that converging point, the Hyper-CEST effect would be at most for vanishing host concentration. We thus set out to determine the limit concentration of CrA detectable near the converging point in dilution series at both temperatures. We chose xenon pressure settings somewhat slightly off the converging points strictly valid for vanishing host concentration because of the expectation of a detection limit in the low nanomolar range.[43,44] At the constant settings $p_{max}$ = 26 mbar at 298 K and $p_{max}$ = 40 mbar at 310 K, respectively, the period $\tau$ for RF irradiation was varied from 0 s to 400 s, and the respective signal decay in dependence of $\tau$, the so-called depletion curve, monitored for the various host concentrations. As shown in Fig. 2B and C, a host concentration of 9 nM or 0.9 nM at 298 K or 310 K, respectively, is manifest in a deviation of the depletion curves for saturation transfer effective or not. Upon further dilution to 0.9 nM and 0.45 nM for 298 K and 310 K, respectively, this separation of the depletion curves disappears, making that host concentrations indistinguishable by the Hyper-CEST experiment. For the concentrations of the dilution series and the parameters of Table 1 the model calculated depletion rates $R + k_{on}$ are in good agreement with the experimental values.

For the samples of the dilution series at 298 K the experimental off-resonant depletion rate was slightly reduced in comparison to the 90 nM sample (Table 1) which may be attributed to a different spin relaxation, *e.g.* due to the grade of sample degassing or glassware-dependent wall relaxation. However, because of the weak dependence of the maxima converging point on $R$, or, *vice versa*, the flatness of $S(\rho,\tau)$ along $\tau$ in the neighborhood of the maximum (Fig. S4, ESI† for 0.9 nM), this deviation is not critical. In contrast, the steep decline of the Hyper-CEST effect towards small $p$ requires investigations at low host concentration to be conducted rather close to the proper $p_{max}$. For example, our polarizer delivers at a xenon partial pressure of $p$ = 5 mbar practically the maximum polarization (~25%).[45] When working at that fixing, by our model the Hyper-CEST effect at 310 K and for 0.9 nM CrA were less

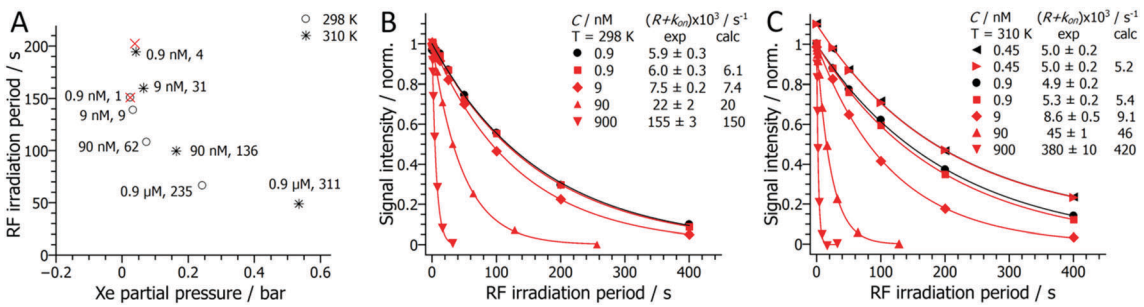


Fig. 2 Optimization of Hyper-CEST performance. (A) Calculated settings of xenon partial pressure and RF irradiation period for maximum Hyper-CEST effect in the CrA–hpXe host–guest system at 298 K (circles) and 310 K (stars), respectively. For each setting, the host concentration and the calculated amplitude of the Hyper-CEST effect, normalized to the value for 0.9 nM and 298 K, are listed. The red cross in each series indicates the converging point for vanishing $C$. (B and C) Show depletion curves with (red) and without (black) saturation transfer effective for the various host concentrations and at 298 K and 310 K, respectively, obtained by exponential fitting to the experimental data. In (C) the depletion curve and measurements for 0.45 nM host concentration are shifted by a constant offset of 0.2 to afford their visibility. Experimental and by the model calculated depletion rates are listed for comparison.

than half compared to the optimal pressure setting of 40 mbar (Fig. S4, ESI†).

### Quantification of sensor concentration

The explicit functional form of the model suggests its usage for quantitation of the host molecule – or contrast agent – present in the solution. Three different approaches are derived from the model for that purpose.

The first method implies solving the model for the total host concentration in terms of the experimental Hyper-CEST effect, denoted $\Delta$, and the parameters entering the model,

$$C(\Delta) = -\ln\left\{1 - \Delta\frac{\exp\{R\tau\}}{A(\rho)}\right\}\frac{1 + K\rho}{(c + k\rho)K\tau}. \qquad (2)$$

In the second approach, the depletion rate $R + k_{on}(\rho)$ instead of the Hyper-CEST effect itself is applied for quantitation, motivated by the rate's linear dependence on the total host concentration. For $\delta$ denoting the experimental depletion rate with saturation transfer effective, the total host concentration by solving the expression for the exchange rate $k_{on}(\rho)$ becomes

$$C(\delta) = (\delta - R)\frac{1 + K\rho}{(c + k\rho)K}. \qquad (3)$$

This approach comes with an inherent statistical averaging due to the determination of the depletion rate $\delta$ by fitting to a number of experimental data points. Furthermore, information about the hyperpolarization process in terms of $A(\rho)$ is not required for data analysis. Lastly, the third mode of quantitation, requiring a reference measurement instead of any knowledge about the polarization process or the host–guest interaction, is devised. The saturation transfer induced depletion rate is for constant sample temperature and free xenon concentration (constant $\rho$) only susceptible to variations in the total host concentration. For a known concentration $C_0$ the depletion rate, denoted $\delta_0$, may be determined. For a sample of unknown host concentration but with a saturation transfer induced depletion rate $\delta$ obtained by identical experimentation, the total host concentration can be revealed by comparison with the reference measurement,

$$C(C_0) = \frac{\delta - R}{\delta_0 - R}C_0. \qquad (4)$$

The quantitative methods proposed here were applied, using the appropriate parameters from Table 1, to the dilution series at 298 K and 310 K to evaluate their performance for different host concentrations and to allow a comparison (Fig. 3). The earlier results of a detection limit of 9 nM at 298 K and 0.9 nM at 310 K (Fig. 2) are confirmed by a match of the estimates with the probed values at reasonable uncertainties. For the minor total host concentrations of 0.9 nM at 298 K and 0.45 nM at 310 K, respectively, just the correct order of magnitude can be deduced by $C(\delta)$ and $C(C_0)$. For the estimation by $C(\Delta)$, however, even such low total host concentration appear to be approximately properly detected with an error margin of $\sim$50%. The probed concentrations are mostly within the error margins of the estimates. The latter are steadily decreasing with increasing host concentration,

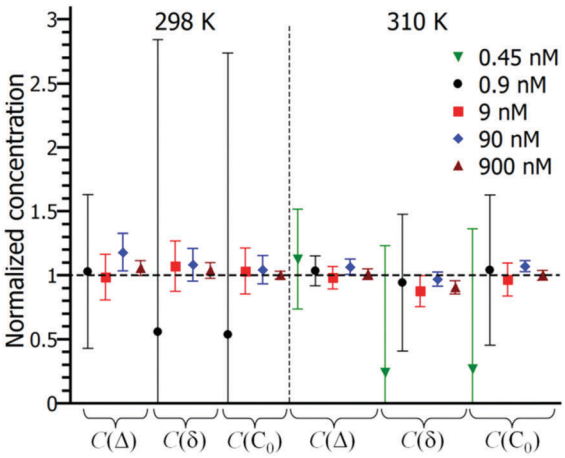


Fig. 3 Numerical values for host quantitation by $C(\Delta)$, $C(\delta)$, and $C(C_0)$, normalized by the probed host concentration (dashed line), at temperatures 298 K and 310 K, respectively. $C(\Delta)$ is the arithmetic mean with SD of the estimates for the individual Hyper-CEST effect $\Delta$ in the respective depletion curve (Fig. 2). Values $\Delta$ were excluded when the expression for $C(\Delta)$ was not solvable or gave physically impossible results (negative argument of logarithm, negative host concentration) and when $\tau$ = 0 (no Hyper-CEST effect). For 90 nM and 900 nM CrA concentration at both temperatures, and additionally 9 nM at 310 K, only depletion curves with saturation transfer effective were conducted (Fig. 2); the respective free xenon signal intensities without saturation transfer were augmented by calculation from the function $Be^{-R\tau}$ and were used for the evaluation of $C(\Delta)$ (with $R$ form Table 1, and $B$ set equal to the first datum of the acquired depletion curve with saturation transfer effective). For $C(C_0)$ the depletion rate at the highest host concentration in the series ($C_0$ = 900 nM) was selected for reference to achieve a possibly low uncertainty in $C_0$. The error margins for estimates $C(\delta)$ and $C(C_0)$ mark the error propagation from the system parameters in Table 1 and the uncertainty in the fitted depletion rate.

as can be expected. The quantifications by $C(\delta)$ and $C(C_0)$ are closely related, the ratio of concentration estimates by the one method is equal to the ratio of corresponding estimates by the other method. At 310 K, however, $C(\delta)$ gives underestimates of the host concentration throughout the series. This artefact can be attributed to a temperature drift in between the samples used for parameter specification and those used for quantitation. Assuming an Arrhenius type of temperature dependence for the rate coefficients $c$ and $k$, which are inversely proportional to $C(\delta)$, the estimates would shift up to the level of those of $C(C_0)$ in the diagram for a half a degree reduced temperature during parameter specification. Such problems are avoided by application of $C(C_0)$ because the reference measurement can be conducted quickly and thus closely to the quantitation measurement in comparison to the more elaborate experimentation for the parameter specification, rendering long term temperature drifts unlikely.

## Discussion

We have developed a model for quantitative measurement and data analysis strategy in biosensing using hyperpolarized xenon and the host CrA. This model is expected to be applicable to the

various host structures in use, *e.g.* the presently explored cucurbit[6]uril (CB6).[18,24,25,46,47] In the model characteristic for the host is the exchange rate $k_{on}$ which, in turn, is governed by the underlying reaction mechanisms. The dissociative and degenerate exchange we have explicitly considered, *i.e.* when xenon encounters a host free of xenon or one already occupied with a xenon atom, respectively, are prevailing for CrA and are expected to occur as well for CB6.[8,9,31] Indeed, these reaction pathways are quite universal for low host and xenon concentrations when collisions of higher order than binary are very unlikely. The numerical values of the corresponding rate coefficients $c$ and $k$ are subject to change with the type of host but the functional dependencies in the model are preserved. Model parameter data do also change for different sample condition, *e.g.* the relaxation rate of free hpXe in human blood is dependent on the blood oxygenation status, and the exchange rates of the CrA–hpXe system are significantly increased in lipid environments in comparison to aqueous solution.[20,48] With the respective parameters appropriately set the evaluation of the model $S(\rho,\tau)$ and the actual sensing performance adapt in parallel.

The functional form of the model, however, may need modifications concerning the spin manipulation. The complete saturation of the magnetization of host-bound hpXe we assumed requires RF irradiation of sufficiently high power for the given xenon residence time within the complex. This was indeed the case here, as is evident by the consistency of our quantitative results and former work on the CrA–hpXe system.[33,34] Practically, complete saturation can be adjusted by the recording of a series of depletion curves with successively increased saturation power until a constant, maximal depletion rate is obtained. However, in cases of short xenon residence time, *e.g.* below a millisecond for CB6, or because of concerns about RF heating, only incomplete saturation may be achieved.[34,44] Hyper-CEST is then affected through a comparatively less effective saturation transfer expressed by the scaling factor $f(\omega,\rho) = \omega^2/(\omega^2 + k_{off}^2)$.[27,33,49] For high saturation power in units of the xenon angular frequency $\omega$ in comparison to the dissociation rate $k_{off}$, $f(\omega,\rho)$ approaches unity indicating the complete saturation regime. Hence, $k_{on}$ needs to be multiplied by $f(\omega,\rho)$ in eqn (1) to account for saturation efficiency in our quantitative model. This modification is uncritical. The rate $k_{off} = c + k\rho$ just shows up once more in the model but is again based on the kinetics parameter $c$ and $k$, while the additional parameter $\omega$ can be straightaway determined, *e.g.* by a flip angle analysis when the saturation irradiation is applied to the free xenon signal. The Hyper-CEST effect is now dependent on $\omega$ in addition to $\rho$ and $\tau$, as is particularly the position of the maximum (ESI†). However, because the scaled saturation rate $k_{on}(\rho)f(\omega,\rho)$ is monotonically growing with $\omega$, for largest Hyper-CEST effect the strongest admissible RF power should be used. Furthermore, the quantification formulas derived from the model also require adjustments to encompass the saturation efficiency. For $C(\Delta)$ and $C(\delta)$ the factor $1/f(\omega,\rho)$ appears on the RHS in eqn (2) and (3), respectively, while $C(C_0)$ remains unchanged.

The model allows determination of the $\rho,\tau$-settings for the maximum Hyper-CEST effect, exemplified here for CrA in aqueous solution. The respective detection limit of 0.9 nM total CrA concentration at 310 K established in the present work is more than one order of magnitude below the limit found recently for a biotinylated CrA derivative at the same temperature but more than two orders above the limit for the more soluble form triacidic acid CrA at 320 K.[43,44] In either case, the free xenon concentration was not specifically considered or optimized. For these, as any other host molecule, the model could help reveal consolidated limits of detection by adjusting $\rho$ and $\tau$ for maximum Hyper-CEST effect and by comparing experimental with model-derived depletion rates (Fig. 2B and C).

The determinations of the total sensor (contrast agent) concentration we presented over the nanomolar range for CrA are, to our knowledge, first evidence and prove the fundamental applicability of hpXe based biosensing in quantitative studies. The quantification concerns the sensor, *i.e.* the hpXe host molecule, possibly targeting the biomarker of interest. The concentration determined thus equals the biomarker concentration when the marker is saturated in the binding to the sensor and the contribution of this complex to saturation transfer can be selected. While in some cases these requirements may be met simply by washing out the excess of the free (not to the biomarker bound) sensor molecules, for applications with xenon exchange in between more than just two pools dedicated experimentation can prove pivotal. Consider biomarker-bound und free sensor molecules, all exchanging bound with free xenon but having a difference $\Delta\omega$ in the resonance frequencies of xenon bound to either type. Typically, $\Delta\omega$ is in a range of a few ppm and up to about 10 ppm in cellular targeting when sensor molecules associate in the lipid environment of the cellular membrane.[15,16,20] When the xenon in the biomarker-bound sensors is resonantly RF irradiated to affect saturation transfer to the free xenon pool, the contribution to the transfer rate of possibly partially RF saturated xenon in the free sensors is $k_{on}\omega^2/(\omega^2 + k_{off}^2 + \Delta\omega^2)$ where $k_{on}$ and $k_{off}$ now denote the xenon exchange rates with respect to the free sensors. The expression is valid when the population in the free xenon pool is dominant and the transverse relaxation rate of encaged xenon is negligible in comparison to $k_{off}$.[27,50] Thus, the poisoning of the saturation transfer from the biomarker-bound sensors by the one from the free sensors could be effectively quenched by adjustment of the saturation power $\omega$. For example, for CrA-based sensors like the ones characterized by the parameters in Table 1 a saturation power of $2\pi$ 50 Hz suffices to achieve practically complete xenon saturation because of the low exchange rate $k_{off}(f(\omega,\rho) = 0.995$ for $k_{off} = 21$ Hz at the pressure setting $p_{Xe} = 0.026$ bar which is optimal at 298 K). Assuming $\Delta\omega = 2$ ppm and a 14.7 T Zeeman field (600 MHz $^1$H Larmor frequency), the resonance frequency of xenon in the free sensors were $2\pi$ 350 Hz away the saturation frequency resonant with the xenon in the biomarker-bound sensors. For similar xenon exchange characteristics whether the sensor is bound or not to the biomarker (identical $k_{on}$, $k_{off}$), the free sensors would contribute a fraction of only 2% to the total saturation transfer rate. Even the very unfavourable cases of completely overlapping resonances of xenon in free and biomarker-bound sensors,

 

respectively, can be principally handled insofar the respective depletion rates ($R + k_{on}$) are sufficiently different. As previously demonstrated for CrA–hpXe systems in various lipid environments with almost identical Larmor frequencies but differing exchange rates for the enclosed xenon, an inverse Laplace transform applied to experimental depletion curves allows disentanglement of the total depletion rate into the proper individual rates stemming from the various xenon pools.[51,52] That rates could subsequently be used to establish the model (eqn (1)) or for input to a quantitative analysis with $C(\delta)$ (eqn (3)).

It is an interesting question in what way the model proposed here for experimentation *in vitro* could be the basis for quantitative evaluations in future *in vivo* molecular imaging. Such an extrapolation must be limited to basic qualitative aspects as the technology is still in its infancy. The passage through and distribution in humans or rodents of xenon administered through inhalation is well understood and the respective parameters, *e.g.* describing the partitioning of xenon across the various tissues, are quite well known due to the applications of radioactive $^{133}$Xe and hpXe in physiology and lung imaging, respectively.[53,54] This information can be rather straightforwardly combined with the saturation transfer from sensor-bound xenon as modelled here.[55] Challenging is the specification of the model parameters (Table 1) under *in vivo* condition, *i.e.* for biosensors locally targeted to specific markers in tissue. One route could be the use of *ex vivo* experimentation, *e.g.* the determination of the rate coefficients and binding constant of xenon exchanging with tissue targeted sensors in an *in vitro* setting under as close as possible physiological conditions.[48] Alternatively, the acquisition of localized Z-spectra with variable saturation power *in vivo* could prove helpful as the exchange rate coefficients can be derived by model fitting.[33] It should be noted that the proposed quantitation approach $C(\delta)$ (eqn (3)) would require – in addition to the partition coefficient for xenon in the relevant tissue – just the knowledge of the exchange rate $k_{off}$ and the sensor–xenon binding constant to facilitate determination of the sensor (contrast agent) concentration by the acquisition of localized depletion curves.

The model proposed here for characterizing biosensor detection by chemically exchanging hpXe is based on the Hyper-CEST effect defined as the difference of signal intensities for saturation transfer effective or not. However, alternative definitions which are also indicative of the biosensor induced saturation transfer may be considered, for example the ratio of the signal intensities as is used in the formation of Hyper-CEST Z-spectra.[33] The model and its applications may than be adapted appropriately. For example, quantitative exploration of Z-spectra data for resonant RF saturation becomes feasible by the expressions $C(\Delta)$, $C(\delta)$ and $C(C_0)$, respectively, when the settings $A(\rho) = 1$ and $R = 0$ are used. It should be noted that for Z-spectra the RF saturation is applied not just resonantly to the encaged hpXe where our formulas apply but is swept over a large frequency band. As discussed above, Hyper-CEST Z-spectra acquired at various RF power enable parameter specification and may thus be particularly helpful – and combine well with the methods proposed here – when sensor-bound hpXe is difficult to detect directly, *e.g.* due to low sensor molecule solubility or xenon affinity.[35]

# Conclusions

This research work furnishes the quantitative assessment of NMR molecular sensors signalling through reversibly bonded hyperpolarized $^{129}$Xe as they are promoted for applications in biomarker targeting and molecular imaging. On grounds of the governing physico-chemical processes and respective parameters (hyperpolarization generation, chemical exchange), which can be specified for the instrumentation and sensor design at hand, the ultra-sensitive sensor detection by saturation transfer can be quantitatively modelled by an analytical expression. Through the adjustment of the amount of xenon and the period of saturation transfer applied in an investigation the model imparts control over the sensor performance, *e.g.* to probe the detection limit; it also permits the achievement of numerical results by transformation of the detected signal (Hyper-CEST effect) into the correct sensor or contrast agent concentration. As the sensor signalling conveys the full information accessible by this biosensing approach, the quantitative analysis also refers to the sensor-targeted biomarkers. Xenon based biosensing is thus advanced towards tailored, quantitative applications. Considering sensors of higher efficacy than the cryptophane-A used in the present study, *e.g.* cucurbiturils or bacterial xenon gas vesicles, quantification in the sub-nanomolar concentration range appears feasible.[44,55] Furthermore, different sensor designs could be compared on grounds of model calculations enabling the best choice beforehand to an actual experimentation, thus ensuring resource efficiency and optimal experimental results. The proposed quantitative modelling should prove advantageous in more sophisticated applications than the basic two-site exchange demonstrated here, including systems with a multiplicity of xenon accessible sensors (multiplexing), and for the extension to *in vivo* experimentation.

# Experimental section

### Sample preparation

Monoacidic acid CrA (purchased from Kangyuan Jiyi Inc.) was dissolved in distilled water. After sonication for one hour at room temperature non-dissolved particles were removed by filtering the solution through pores of 2 μm diameter. The concentration of CrA in the saturated solution was measured by UV-Vis spectroscopy using the experimentally determined molar attenuation coefficient of 16 200 $M^{-1}cm^{-1}$. Solutions of around 10 μM CrA were obtained regularly in this manner. For the dilution series, a stock solution was prepared and stepwise further diluted.

### Parameter specification

The CrA–xenon association constant in water, $K$, was determined using CrA fluorescence quenching by xenon binding as described in ref. 32 (ESI). The association constants for CrA with $N_2$ and He which were also present in the gas mixture bubbled through the sample were analogously determined and taken into account (no measureable effect for He). The rate coefficients $c$ and $k$ for the CrA–xenon exchange kinetics in

water at 298 K were, together with their uncertainties, previously determined using exchange spectroscopy and are taken over in the present work.[34] The respective values at 310 K were determined by similar experimentation (ESI†). At each setting of the xenon partial pressure used for measuring the $\rho,\tau$-dependent Hyper-CEST effect (Fig. 1C) also a standard one-dimensional xenon spectrum was acquired. The respective signal intensities of freely dissolved xenon are a measure of the function $A(\rho)$ describing the polarizer performance in dependence of the xenon gas partial pressure and were used for determination of the polarization parameter $\alpha$ (ESI†). The relaxation and direct saturation rate, $R$, is for the data on the $\rho,\tau$-dependence of the Hyper-CEST effect (Fig. 1C) the arithmetic mean with SD of the seven off-resonant depletion rates for each individual xenon partial pressure setting (0.01 to 0.8 bar). For the dilution series at 298 K or 310 K (Fig. 2B and C), $R$ is the arithmetic mean of the off-resonant depletion rates for 0.9 and 9 nM CrA or 0.45 and 0.9 nM CrA, respectively, with the uncertainty given by the propagation of the error in the individual rates due to mono-exponential fitting. The solubility $s$ with uncertainty was taken from the literature but temperature fluctuations in the sample solution of half a degree additionally assumed.[40]

### HpXe NMR experiments

NMR experiments were performed on a 7 T spectrometer (Bruker Corporation) equipped with a double resonant probe for excitation and detection of $^{1}$H and $^{129}$Xe at 300 MHz and 83 MHz, respectively. The sample was maintained at 298 K or 310 K during the experiments using temperature controlled air flow. The signal of freely dissolved $^{129}$Xe was used for referencing the chemical shift scale and set to 196 ppm. For the measurements of the Hyper-CEST effect (Fig. 1C) and depletion curves (Fig. 2B and C) RF irradiation of an amplitude of 500 Hz in units of the xenon precession frequency was applied for a variable period $\tau$ in the range of 0 s to 400 s and subsequently the free xenon magnetization selectively excited by a Gaussian RF pulse of 1 ms length for signal acquisition. Depletion rates were obtained by a non-linear least squares fit of a mono-exponential function to the signal intensities in dependence of the RF irradiation period $\tau$ (Fig. 2B and C) using the software QtiPlot. The error margins of the rates are the standard error in the fit. The hyperpolarized $^{129}$Xe was generated by a custom-designed continuous-flow polarizer using spin-exchange-optical pumping.[44] The gas mixture of hpXe, nitrogen and helium at the outlet of the polarizer was transferred *via* a PFE hose to the NMR magnet and directly bubbled into the sample solution.

## Conflicts of interest

There are no conflicts of interest to declare.

## Acknowledgements

This work was funded by the Bundesministerium für Bildung und Forschung (01EZ1010A), EURAMET and the European Union (EMRP grant HLT-10), and the German Science Foundation (TRR 676-A2). The authors are grateful to A. Kiryutin for sample purity assessment.

## References

1 M. L. Quilin and B. W. Matthews, *Acta Crystallogr., Sect. D: Biol. Crystallogr.*, 2002, **58**, 97–103.
2 A. M. Rubin, S.-Y. Lee, E. J. Ruiz, A. Pines and D. Wemmer, *J. Mol. Biol.*, 2002, **322**, 425–440.
3 L. Dubois, P. Da Silva, C. Landon, J. G. Huber, M. Ponchet, F. Vovelle, P. Berthault and H. Desveaux, *J. Am. Chem. Soc.*, 2004, **126**, 15738–15746.
4 Y. Bai, Y. Wang, M. Goulian, A. Dirks and I. J. Dmochowski, *Chem. Sci.*, 2014, **5**, 3197–3203.
5 C. Groeger, A. Moeglich, M. Pons, B. Koch, W. Hengstenberg, H. R. Kalbitzer and E. Brunner, *J. Am. Chem. Soc.*, 2003, **125**, 8726–8727.
6 T. J. Lowery, S. M. Rubin, E. J. Ruiz, A. Pines and D. Wemmer, *Angew. Chem., Int. Ed.*, 2004, **43**, 6320–6322.
7 N. Branda, R. M. Grotzfeld, C. Valdés and J. Rebek, *J. Am. Chem. Soc.*, 1995, **117**, 85–88.
8 K. Bartik, M. Luhmer, J.-P. Dutasta, A. Collet and J. Reisse, *J. Am. Chem. Soc.*, 1998, **120**, 784–791.
9 M. E. Haouaj, M. Luhmer, Y. H. Ko, K. Kim and K. Bartik, *J. Chem. Soc., Perkin Trans. 2*, 2001, 804–807.
10 D. Raferty, *Annu. Rep. NMR Spectrosc.*, 2006, **57**, 206–263.
11 V.-V. Telkki, J. Lounila and J. Jokisaari, in *Hyperpolarized Xenon-129 Magnetic Resonance: Concepts, Production, Techniques and Applications*, ed. T. Meersmann and E. Brunner, The Royal Society of Chemistry, Cambridge, 2015, ch. 10, pp. 185–199.
12 B. M. Goodson, *J. Magn. Reson.*, 2002, **155**, 157–216.
13 T. G. Walker and W. Happer, *Rev. Mod. Phys.*, 1997, **69**, 629–642.
14 M. M. Spence, S. M. Rubin, I. E. Dimitrov, E. J. Ruiz, D. E. Wemmer, A. Pines, S. Q. Yao, F. Tian and P. G. Schultz, *Proc. Natl. Acad. Sci. U. S. A.*, 2001, **98**, 10654–10657.
15 O. Taratula and I. J. Dmochowski, *Curr. Opin. Chem. Biol.*, 2010, **14**, 97–104.
16 H. M. Rose, C. Witte, F. Rossella, S. Klippel, C. Freund and L. Schröder, *Proc. Natl. Acad. Sci. U. S. A.*, 2014, **111**, 11697–11702.
17 Y. Wang and I. J. Dmochowski, *Acc. Chem. Res.*, 2016, **49**, 2179–2187.
18 F. T. Hane, T. Li, P. Smylie, R. M. Pellizzari, J. A. Plata, B. DeBoef and M. S. Albert, *Sci. Rep.*, 2017, **7**, 41027.
19 M. M. Spence, E. J. Ruiz, S. M. Rubin, T. J. Lowery, N. Winssinger, P. G. Schultz, D. E. Wemmer and A. Pines, *J. Am. Chem. Soc.*, 2004, **126**, 15287–15294.
20 T. Meldrum, L. Schroeder, P. Denger, D. E. Wemmer and A. Pines, *J. Magn. Reson.*, 2010, **205**, 242–246.
21 L. Schroeder, T. J. Lowery, C. Hilty, D. E. Wemmer and A. Pines, *Science*, 2006, **314**, 446–449.
22 A. Schlundt, W. Kilian, M. Beyermann, J. Sticht, S. Günther, S. Höpner, K. Falk, O. Roetzschke, L. Mitschang and C. Freund, *Angew. Chem., Int. Ed.*, 2009, **48**, 4142–4145.

23 S. Klippel, J. Döpfert, J. Jayapaul, M. Kunth, F. Rossella, M. Schnurr, C. Witte, C. Freund and L. Schröder, *Angew. Chem., Int. Ed.*, 2014, **53**, 493–496.
24 Y. Wang, B. W. Roose, J. P. Philbin, J. L. Doman and I. J. Dmochowski, *Angew. Chem., Int. Ed.*, 2016, **55**, 1733–1736.
25 J. A. Finbloom, C. C. Slack, C. J. Bruns, K. Jeong, D. E. Wemmer, A. Pines and M. B. Francis, *Chem. Commun.*, 2016, **52**, 3119–3122.
26 M. Schnurr, K. Sydow, H. M. Rose, M. Dathe and L. Schroeder, *Adv. Healthcare Mater.*, 2015, **4**, 40–45.
27 M. Zaiss, M. Schnurr and P. Bachert, *J. Chem. Phys.*, 2012, **136**, 144106.
28 M. S. Freeman, K. Emami and B. Driehuys, *Phys. Rev. A: At., Mol., Opt. Phys.*, 2014, **90**, 023406.
29 G. Norquay, S. R. Parnell, X. Xu, J. Parra-Robles and J. M. Wild, *J. Appl. Phys.*, 2013, **113**, 044908.
30 J. S. Six, T. Hughes-Riley, K. F. Stupic, G. E. Pavlovskaya and T. Meersmann, *PLoS One*, 2012, **7**, e49927.
31 S. Korchak, W. Kilian and L. Mitschang, *Chem. Commun.*, 2015, **51**, 1721–1724.
32 P. A. Hill, Q. Wei, R. Eckenhoff and I. J. Dmochowski, *J. Am. Chem. Soc.*, 2007, **129**, 9262–9263.
33 M. Kunth, C. Witte and L. Schroeder, *J. Chem. Phys.*, 2014, **141**, 194202.
34 S. Korchak, W. Kilian, L. Schröder and L. Mitschang, *J. Magn. Reson.*, 2016, **265**, 139–145.
35 M. Kunth, C. Witte, A. Hennig and L. Schröder, *Chem. Sci.*, 2015, **6**, 6069–6075.
36 T. Brotin, A. Lesage, L. Emsley and A. Collet, *J. Am. Chem. Soc.*, 2000, **122**, 1171–1174.
37 E. Dubost, J.-P. Dognon, B. Rousseau, G. Milanole, C. Dugave, Y. Boulard, E. Léonce, C. Boutin and P. Berthault, *Angew. Chem., Int. Ed.*, 2014, **53**, 9837–9840.
38 O. Taratula, P. A. Hill, N. S. Khan, P. J. Carroll and I. J. Dmochowski, *Nat. Commun.*, 2010, **1**, 148.
39 L. Gao, W. Liu, O.-S. Lee, I. J. Dmochowski and J. G. Saven, *Chem. Sci.*, 2015, **6**, 7238–7248.
40 H. L. Clever, in *Solubility Data Series: Krypton, Xenon and Radon – Gas Solubilities*, ed. A. S. Kertes and H. L. Clever, Pergamon Press, Oxford, 1979, vol. 2, pp. 134–227.
41 K. Kitani, *Scand. J. Clin. Lab. Invest.*, 1972, **29**, 167–172.
42 L. H. Gevantman, in *CRC Handbook of Chemistry and Physics: Solubility of selected gases in water*, ed. W. M. Haynes, CrC Press, Boca Raton, 94th edn, 2013, ch. 5, pp. 149–152.
43 L. Schröder, T. Meldrum, M. Smith, T. J. Lowery, D. E. Wemmer and A. Pines, *Phys. Rev. Lett.*, 2008, **100**, 257603.
44 Y. Bai, P. A. Hill and I. J. Dmochowski, *Anal. Chem.*, 2012, **84**, 9935–9941.
45 S. Korchak, W. Kilian and L. Mitschang, *Appl. Magn. Reson.*, 2013, **44**, 65–80.
46 Y. Wang and I. J. Dmochowski, *Chem. Commun.*, 2015, **51**, 8982–8985.
47 F. T. Hane, P. S. Smylie, T. Li, J. Ruberto, K. Dowhos, I. Ball, B. Tomanek, B. DeBoef and M. S. Albert, *Contrast Media Mol. Imaging*, 2016, **11**, 285–290.
48 G. Norquay, G. Leung, N. J. Stewart, G. M. Tozer, J. Wolber and J. M. Wild, *Magn. Reson. Med.*, 2015, **4**, 303–311.
49 M. Kunth, C. Witte and L. Schroeder, *NMR Biomed.*, 2015, **28**, 601–606.
50 O. Trott and A. G. Palmer, *J. Magn. Reson.*, 2004, **170**, 104–112.
51 M. Schnurr, C. Witte and L. Schroeder, *Phys. Chem. Chem. Phys.*, 2013, **15**, 14178–14181.
52 M. Schnurr, C. Witte and L. Schroeder, *Biophys. J.*, 2014, **106**, 1301–1308.
53 C. C. Martin, R. F. Williams, J.-H. Gao, L. D. H. Nickerson, B. S. Jinhu Xiong and P. T. Fox, *J. Magn. Reson. Imaging*, 1997, **7**, 848–854.
54 X. Zhou, M. L. Mazzanti, J. J. Chen, Y.-S. Tzeng, J. K. Mansour, J. D. Gereige, A. K. Venkatesh, Y. Sun, R. F. Mulkern and A. S. Albert, *NMR Biomed.*, 2008, **21**, 217–225.
55 M. G. Shapiro, R. M. Ramirez, L. J. Sperling, G. Sun, J. Sun, A. Pines, D. V. Schaffer and V. K. Bajaj, *Nat. Chem.*, 2014, **6**, 629–634.